

Chapter 4

Multichannel quantum defect treatment of cold collisions

Chapter 2 presented the textbook approach for scattering theory of cold atoms, deriving a set of coupled-channel Schrödinger equations which describe the collision dynamics. Brute-force numerical techniques for solving these equations were developed in Chapter 3. One job that falls to the cold collision practitioner is refining the Born-Oppenheimer potentials such that theoretical calculations agree with experiment. This usually requires the solution of the scattering equations throughout a large parameter space that consists of the Born-Oppenheimer parameters: singlet a_s and triplet a_t scattering lengths, and the C_6 dispersion coefficient. In addition, the calculations often must be performed for a number of magnetic bias fields B and collision energies E . Although the numerical algorithms presented in Chapter 3 are reasonably fast, this still becomes a time consuming project when many thousands of calculations are needed to bound the parameter space, as is frequently the case.

To alleviate this difficulty, our understanding of cold collision physics can be exploited to develop a more compact and efficient framework for solution of the scattering equations. The method outlined here is a fully-developed theory for spin-exchange collisions. The magnetic dipole interaction is neglected throughout this chapter. The techniques developed here should also allow dipolar effects to be calculated conveniently within perturbation theory, though this has not yet been implemented. Referring back to Fig. 2.1, it is obvious that the collision partners experience two very different energy scales in the course of a scattering event. At small R , the Born-Oppenheimer potentials are very deep compared to typical collision energies and the relative kinetic energy of the pair is large. At large R , the hyperfine energy sets the scale. The energy scale of interest for cold ground state collisions ranges up to a few mK. Over this range, the small R wave functions do not change appreciably (see Fig. 4.1) implying that, to a good approximation, this part of the problem is nearly energy-independent. This in itself represents a huge computational savings because the spin-exchange coupling occurs in this small R region (see Fig. 3.2) and only needs to be calculated for a few values (or even just a single value) of E . The energy dependence of the final scattering matrices derives from the large R evolution of the wave function where the channels are uncoupled;

the solutions in this region can therefore be obtained in terms of single-channel solutions to a simple radial Schrödinger equation. In addition, the large R solutions can be parameterized such that the single channel equations need to be solved only once as a function of energy. Moreover, we will see that the parameterization can be made essentially atom-independent. The final scattering solutions can then be obtained through the manipulation of a few small matrices.

This approach has its origins in Seaton's[80] multichannel quantum defect theory (MQDT) and in multichannel effective range theory[81]. I will refer to the method as multichannel spectroscopy or sometimes simply MQDT. It has proven to be a powerful yet simple theoretical tool for describing multichannel collisions and half-collisions, in contexts such as Rydberg electron motion[23] in the field of a structured ionic core. The theory is well known and has been applied to cold alkali collisions by other groups[82, 83, 84, 85, 86, 87, 88]. However, the formulation presented here has two new key developments[89]; i) a new standardization of the long-range field properties which allows a nearly atom-independent parameterization, and ii) a recoupling frame transformation (FT) approximation. The FT approximation combined with the long-range MQDT parameters reproduces the multichannel collision physics, with reasonable accuracy for most systems, completely in terms of single channel parameters. In addition to increased numerical efficiency, MQDT provides a great deal of insight. The techniques developed here are used in later chapters to explain certain aspects of cold collision dynamics.

The structure of this chapter is as follows: In section 4.1, accurate solutions of the Schrödinger equation in the presence of a long-range potential are described. The parameters that connect these solutions with free-particle solutions (j_l, n_l) at $R \rightarrow \infty$ are defined and evaluated. In Section 4.2 the matrix equations that allow one to connect the small and large R solutions and ultimately derive an \underline{S} -matrix are developed. In addition, it is shown how to construct energy-normalized scattering wave functions from the reference wave functions and long-range parameters. A frame transformation approximation for the short-range reaction matrix is presented in Section 4.3 and finally, example calculations illustrating the MQDT approach are presented in Section 4.4.

4.1 Reference wave functions

In multichannel spectroscopy, the key idea is to express scattering observables in terms of a real, linearly independent base pair (f^0, g^0) of solutions to the radial Schrödinger equation in the appropriate long-range potential. The long-range potential applicable for ground state spin-exchange collisions is

$$V^{lr}(R) = -\frac{C_6}{R^6} - \frac{C_8}{R^8} - \frac{C_{10}}{R^{10}}. \quad (4.1)$$

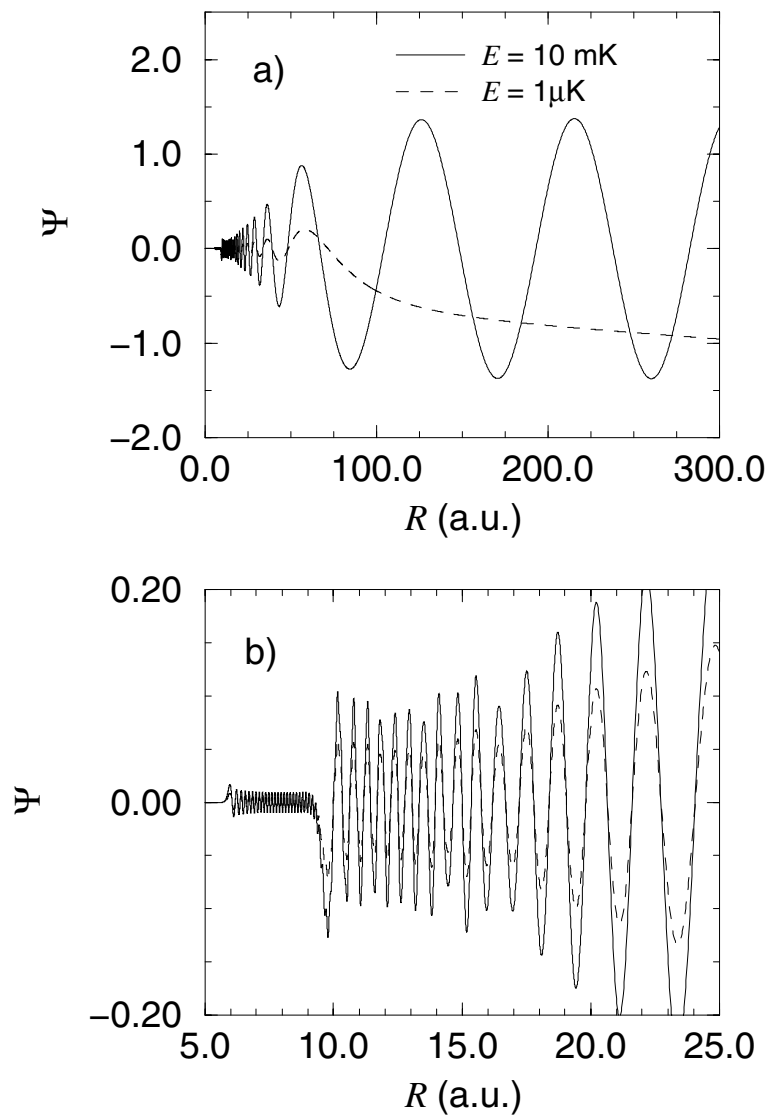


Figure 4.1: Component of a multichannel wave function calculated at two collision energies $E = 1\mu\text{K}$ and $E = 10\text{mK}$. Top figure a) shows the strong energy dependence of the long range part of the wave function. Bottom figure b) is a blowup of the small R part of the wave function. Except for an overall normalization constant the two wave functions are almost identical.

$V^{lr}(R)$ is the exact form of the long range potentials for both singlet and triplet Born-Oppenheimer states once the long-range exchange interaction becomes exponentially small. This occurs at roughly $R \geq 30$ Bohr in all the alkalis (see Fig. 4.2). An advantage to the numerical approach presented here is the fact that this methodology is not restricted to the form 4.1 of $V^{lr}(R)$. The theory can be easily extended to incorporate retardation effects or other forms for the long range potentials.

In Section 4.1.1 the Milne phase amplitude method is used to generate the energy-analytic base pair of radial solutions (f^0, g^0). This pair is then standardized making the MQDT parameters portable from atom to atom. Section 4.1.2 presents transformations that allow the base pair (f^0, g^0) to be written in terms of an asymptotic energy-normalized base pair (f, g) required by scattering theory. The four long-range parameters needed for these transformations are defined and evaluated. Their low-energy properties are then detailed in section 4.1.3.

4.1.1 Milne equation

A convenient, exact representation of (f^0, g^0) can be obtained within the Milne[90] phase-amplitude method, details of which are provided in Ref.[91, 92]:

$$\begin{aligned} f^0(\varepsilon, l, R) &= \sqrt{\frac{2\mu}{\pi}} \alpha(R) \sin \left(\int_{R_x}^R \frac{dR'}{\alpha^2(R')} + b_l \right) \\ g^0(\varepsilon, l, R) &= -\sqrt{\frac{2\mu}{\pi}} \alpha(R) \cos \left(\int_{R_x}^R \frac{dR'}{\alpha^2(R')} + b_l \right) . \end{aligned} \quad (4.2)$$

The Milne amplitude $\alpha(R)$ is a particular solution of the Milne nonlinear equation

$$\frac{\partial^2 \alpha}{\partial R^2} + k^2(R) \alpha(R) = \alpha^{-3}(R) . \quad (4.3)$$

where the R -dependent wave number is defined as

$$k(R) = \sqrt{2\mu(\varepsilon - \frac{l(l+1)}{2\mu R^2} - V^{lr})} . \quad (4.4)$$

Eq. 4.3 is solved with a predictor-corrector method[62] subject to WKB-like boundary conditions at some small fixed radius R_x (generally chosen to be $R_x = 10$ a.u.), namely,

$$\begin{aligned} \alpha(R_x) &= k(R_x)^{-1/2} \\ \alpha'(R_x) &= \frac{\partial}{\partial R} [k(R_x)^{-1/2}] . \end{aligned} \quad (4.5)$$

WKB-type boundary conditions are not strictly necessary, however, Korsch and Laurent have shown[93] that this provides optimal smoothness in the radial and energy variations of α . The choice of $R_x = 10$ a.u. is somewhat arbitrary, all

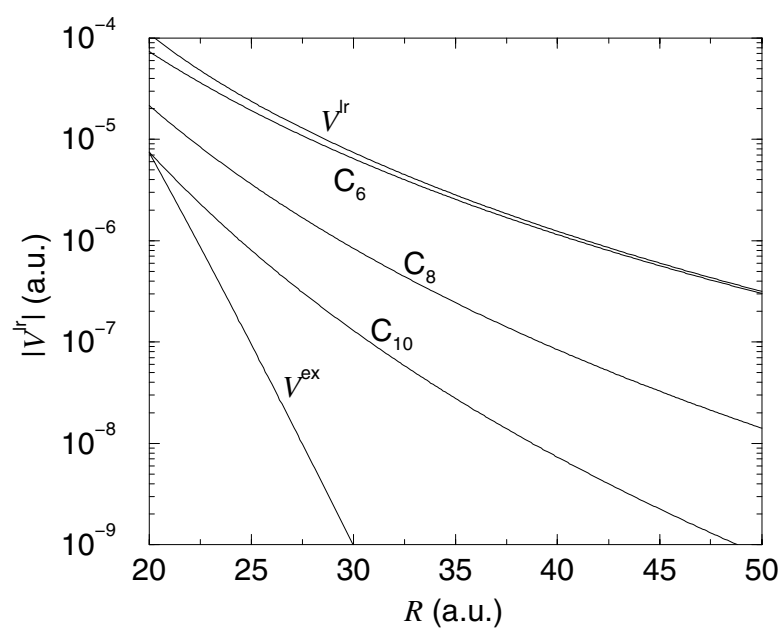


Figure 4.2: Contributions to the the Rb_2 long range potential V^{lr} . These include the three dispersion terms, each of which is labeled by its coefficient C_n . The long-range exchange term V^{ex} which is not included in V^{lr} is also shown.

one requires is that $V^{lr}(R_x)$ is deep enough that the semi-classical approximation is reasonably good where the boundary conditions are applied. An example of the base pair (f^0, g^0) derived from the “smooth” Milne amplitude and phase $\phi(R) = \int \alpha^{-2}(R')dR'$ is shown in Fig. 4.3.

The **energy independent** phase shift b_l in Eq. 4.2 standardizes the low-energy asymptotic structure of (f^0, g^0) . Its introduction allows us to develop a nearly atom-independent parameterization of the long-range field properties (subsection 4.1.2). The phase shift b_l is chosen such that

$$f^0(\varepsilon = 0, l, R) \xrightarrow{R \rightarrow \infty} \text{const} \times R^{l+1}. \quad (4.6)$$

In the s -wave limit this is equivalent to demanding that the scattering length of f^0 must vanish. The standardization phase is determined by integrating the Milne equation from R_x to $R_{max} \sim 200$ Bohr at zero energy and then equating the logarithmic derivative of $f^0(\varepsilon = 0, l, R_{max})$ with the logarithmic derivative of the zero energy solutions of the Schrödinger equation in the presence of a van der Waals potential (i.e., $V^{lr} = -C_6/R^6$ which is valid beyond $R \sim 200$ Bohr). These solutions[24], $\Psi \sim R^{1/2}J_{\pm\nu}(x)$, are given in terms of Bessel functions of fractional order ν . One independent solution, with $\nu = -(2l + 1)/4$, has the proper asymptotic behavior R^{l+1} . Here, x represents a rescaled variable $x = \sqrt{\frac{\mu C_6}{2}}R^{-2}$. The final expression for the standardization phase is

$$b_l = -\phi(R_{max}) + \tan^{-1} \left[\frac{2R_{max}J_\nu(x)}{\alpha^2(R_{max})[J_\nu(x) + 2R_{max}J'_\nu(x)] - 2R_{max}J_\nu(x)\alpha(R_{max})\alpha'(R_{max})} \right] \quad (4.7)$$

The derivative of the Bessel function $J'_\nu(x)$ is taken with respect to R . Setting large R boundary conditions for f^0 is contrary to the “standard” MQDT approach[80, 82, 83, 84, 85, 86, 87, 88] which requires f^0 to vanish as $R \rightarrow 0$. However, the reference potential V^{lr} is not physical inside $R \leq 30$ a.u. and the base pair (f^0, g^0) is never used there. This provides a very clean separation of the small and large R physics, as well as a simple standardization of the long range parameters.

4.1.2 Calculating the MQDT parameters

We ultimately want a scattering solution normalized to $\delta(E - E')$. This is obtained by introducing a second energy normalized base pair (f, g) , which are non-analytic functions of energy. The energy-normalized base pair is related to (f^0, g^0) through the transformation

$$\begin{pmatrix} f(R) \\ g(R) \end{pmatrix} = \begin{pmatrix} A^{1/2} & 0 \\ A^{-1/2}\mathcal{G} & A^{-1/2} \end{pmatrix} \begin{pmatrix} f^0(R) \\ g^0(R) \end{pmatrix}. \quad (4.8)$$

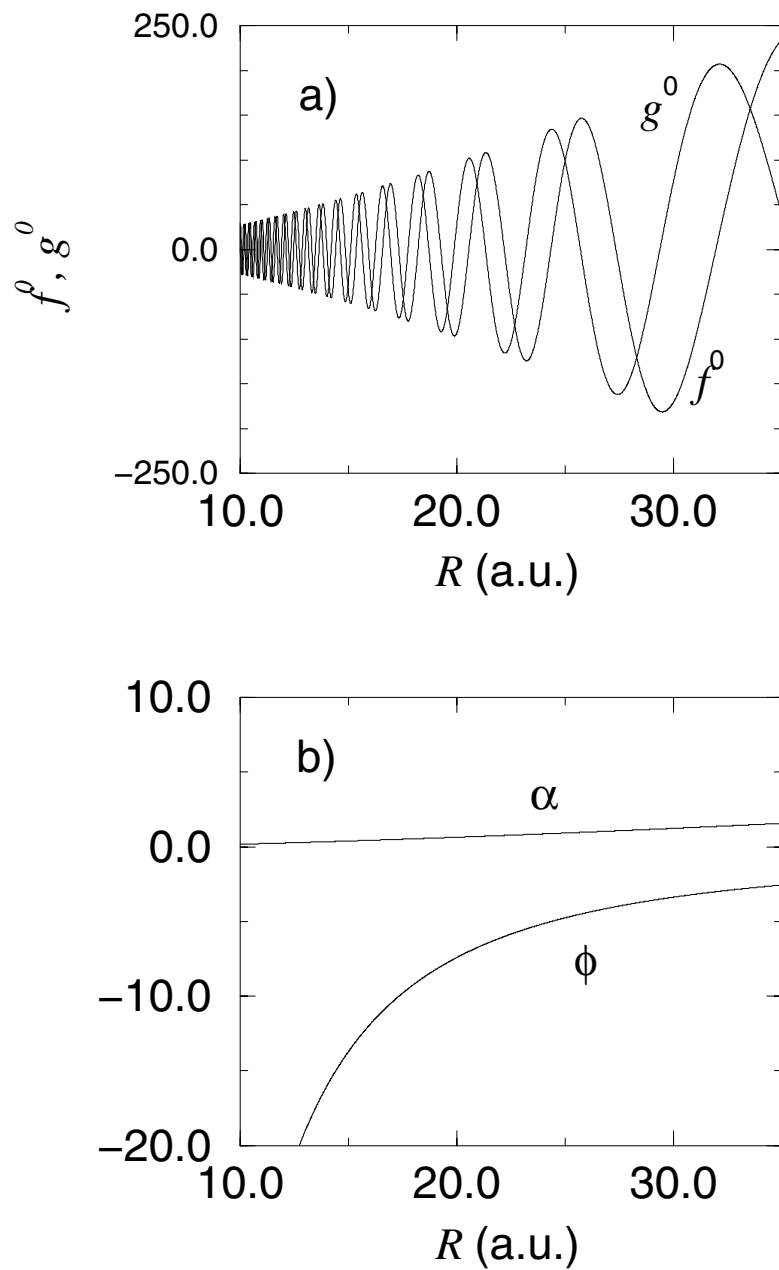


Figure 4.3: a) The base pair (f^0, g^0) are shown as a function of R . These were constructed from the Milne amplitude α and phase ϕ shown in b).

The MQDT parameters $A(\varepsilon, l)$ and $\mathcal{G}(\varepsilon, l)$ are independent of R and are essentially normalization factors. The new base pair are also mathematically correct solutions of the Schrödinger equation in the presence of the long range-field V^{lr} . Moreover, (f, g) can be expressed simply in terms of the energy-normalized spherical Bessel and Neumann functions at large R ,

$$\begin{aligned} f(R) &\xrightarrow{R \rightarrow \infty} kR\sqrt{2\mu/\pi k} (j_l(kR) \cos \eta - n_l(kR) \sin \eta) \\ g(R) &\xrightarrow{R \rightarrow \infty} kR\sqrt{2\mu/\pi k} (j_l(kR) \sin \eta + n_l(kR) \cos \eta) . \end{aligned} \quad (4.9)$$

The non-analytic solutions (f, g) incur a phase-shift $\eta(\varepsilon, l)$ (due to the presence of V^{lr}) relative to the free particle solutions. These three parameters (A, \mathcal{G}, η) summarize all that is needed to characterize the positive energy solutions. They are obtained by integrating Eq. 4.3 from R_x to $R_\infty \sim 10^4$ Bohr at energy ε . It is only necessary to construct the energy-analytic base pair (Eq. 4.2) and spherical Bessel and Neumann solutions at R_∞ . Using Eq. 4.8 and 4.9, the MQDT parameters can be related to the Wronskians $W(\dots)$ of these two sets of linearly independent solutions through the following relationships:

$$\begin{aligned} \tan \eta &= W(f^0, f^s)/W(f^0, g^s) \\ A &= - \left[\frac{W(g^0, f^s) - \tan \eta W(g^0, g^s)}{W(f^0, g^s) + \tan \eta W(f^0, f^s)} \right] \\ \mathcal{G} &= - \left[\frac{W(g^0, g^s) + \tan \eta W(g^0, f^s)}{W(f^0, g^s) + \tan \eta W(f^0, f^s)} \right] . \end{aligned} \quad (4.10)$$

Here, f^s, g^s are the energy normalized spherical Bessel and Neumann functions (defined in subsection 3.2). The last long-range parameter that will be needed is a negative energy phase $\beta(\varepsilon, l)$, which represents the phase accumulated in V^{lr} ,

$$\beta(\varepsilon, l) = \int_{R_x}^{\infty} \alpha(R')^{-2} dR' + b_l . \quad (4.11)$$

The standardization of f^0 allows us to tabulate these long-range field parameters once and for all as functions of the single parameter $\gamma = (2\mu)^3 C_6 \varepsilon^2$, in a.u. This scaling is strictly valid only for a pure van der Waals long-range potential, but in practice holds to a good approximation for the above form of V^{lr} . Examples of the standardized s - through f -wave parameters are shown in Fig. 4.4. The standardization proposed here begins to break down for partial waves greater than $l = 2$ for different atoms (i.e., when you vary the mass and V^{lr} parameters) and beyond $l = 3$ when one simply varies C_6 . In addition, the current procedure for determining the nonzero l parameters at very low positive energies is numerically unstable. Both of these problems are likely linked to the large exponential growth

of the Milne amplitude in the classically forbidden region, which eventually leads to a linearly **dependent** base pair. A possible remedy would be to incorporate the analytical van der Waals solutions at finite energy derived in Ref.[88]. This would circumvent most of the exponential growth because it would not be necessary to integrate as far into the classically forbidden region. These issues will be the subject of a future study.

4.1.3 Low energy behavior of the long-range parameters

In the limit of zero energy, the asymptotic solutions for both positive and negative energy versions of the reference wave functions (f^0, g^0) should be equivalent. However, the long-range nature of the potential makes this difficult to achieve numerically. Therefore, it is preferable to develop an analytical connection formula to bridge this gap. The asymptotic form of the positive energy base pair (f^0, g^0) can be written (using equations 4.8 and 4.9) as the following,

$$\begin{aligned} f^0 &\xrightarrow{R \rightarrow \infty} \sqrt{\frac{2\mu}{\pi k}} A^{-1/2} \sin(kR - l\pi/2 + \eta) \\ g^0 &\xrightarrow{R \rightarrow \infty} -\sqrt{\frac{2\mu}{\pi k}} [A^{1/2} \cos(kR - l\pi/2 + \eta) + A^{-1/2} \mathcal{G} \sin(kR - l\pi/2 + \eta)] . \end{aligned} \quad (4.12)$$

In the zero energy limit, f^0 becomes simply

$$f^0 \xrightarrow{R \rightarrow \infty} \sqrt{\frac{2\mu}{\pi}} A^{-1/2} [k^{l+1/2} R^{l+1} \cos \eta - k^{-(l+1/2)} R^{-l} \sin \eta] = R^{2l+1}/C . \quad (4.13)$$

Our standardization of f^0 forces its asymptotic behavior to be $f^0 \rightarrow R^{l+1}/C$. Therefore in the low-energy limit, $A \rightarrow C^2 k^{2l+1}$ and $\eta \rightarrow 0$. In addition, we find empirically that \mathcal{G} goes to a constant value, $\mathcal{G}_l \rightarrow \mathcal{G}_l(0)$. The Wigner threshold properties of the \underline{S} -matrix are ultimately obtained from this low-energy behavior of A . We can now use these relationships to write down the low-energy limit for g^0 , which is

$$g^0 \rightarrow \frac{C}{R^l} - \frac{\mathcal{G}(0)}{C} R^{l+1} . \quad (4.14)$$

The negative energy solutions are written in terms of the Milne phase ($\beta = \phi + b_l$) and amplitude α as originally given in Eq. 4.2. Using $\frac{2\mu}{\pi} \alpha^2 = (f^0)^2 + (g^0)^2$ and equations 4.13 and 4.14, we find

$$\alpha^2 \xrightarrow{R \rightarrow \infty} \frac{R^{2l+2}}{C^2} [1 + \mathcal{G}^2(0)] \quad (4.15)$$

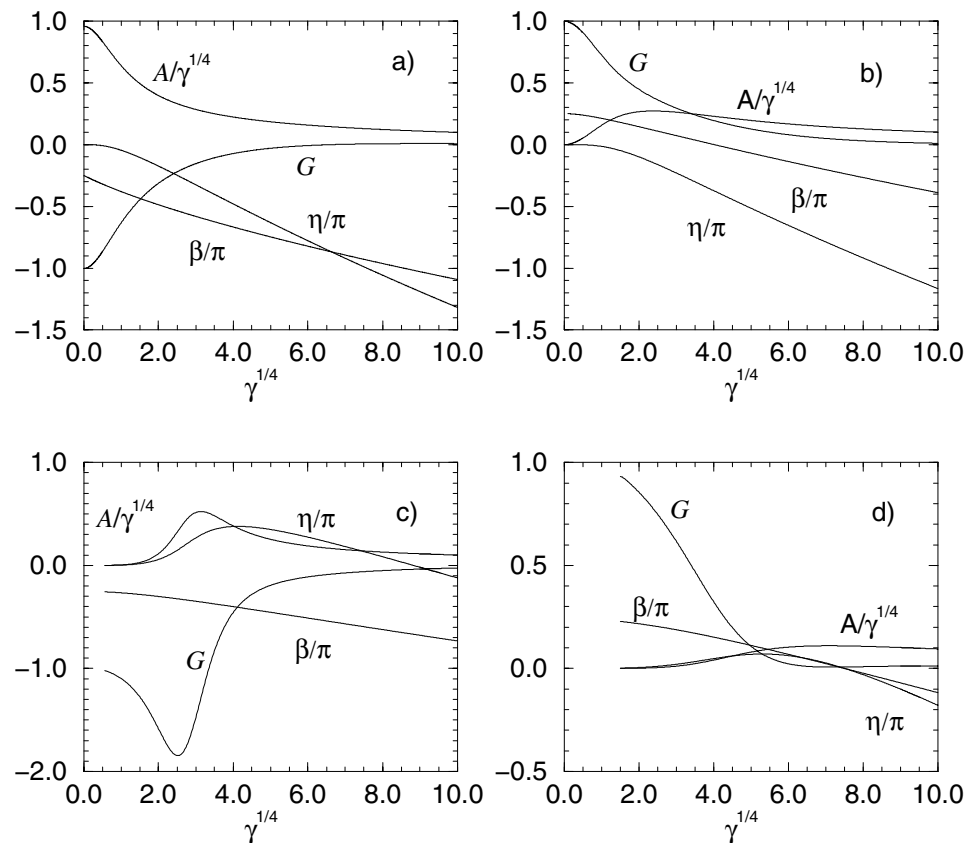


Figure 4.4: The four long-range standardized MQDT parameters are shown for a) $l = 0$, b) $l = 1$, c) $l = 2$, and d) $l = 3$ partial waves as a function of the parameter $\gamma^{1/4} = (2\mu C_6)^{1/4}|k|$. On this scale, the parameters for $l = 0 - 2$ are nearly indistinguishable for all the alkalis. As a point of reference, the energy range $E = 1 \mu\text{K} - 1 \text{ mK}$ for a ^{87}Rb atom corresponds with the range $\gamma^{1/4} = 0.1-3.7$.

and the negative energy reference function becomes

$$f^0 \rightarrow \sqrt{\frac{2\mu}{\pi}} \frac{R^{l+1}}{C} [1 + \mathcal{G}^2(0)]^{1/2} \sin \beta(0) . \quad (4.16)$$

Comparing f^0 in equations 4.13 and 4.16 provides the connection between the positive and negative energy parameters,

$$|\sin \beta(0, l)| = [1 + \mathcal{G}^2(0, l)]^{-1/2} . \quad (4.17)$$

The correct threshold energy behavior of the elastic scattering cross section is obtained if β satisfies this condition. This is illustrated in Fig. 4.5.

It is useful to have s -wave values for both A and \mathcal{G} in the zero energy limit, as these will be related to the scattering length in the next section. The constants $C^2 = c(2\mu C_6)^{1/4}$, $\mathcal{G}(0)$ and $\beta(0)$ are tabulated for the nominal set of dispersion parameters for each alkali atom (except Fr) in Table 4.1.

Table 4.1: Zero energy values of the s -wave long-range parameters. A is related to the constant c through the expression $A/k = c(2\mu C_6)^{1/4}$. Equation 4.17 is used to determine $\beta(0)$.

Atom	c	$\mathcal{G}(0)$	$\beta(0)$
Li	0.96023	-1.0091	-0.78087
Na	0.95857	-1.0055	-0.78266
K	0.95775	-1.0037	-0.78355
Rb	0.95722	-1.0026	-0.78410
Cs	0.95701	-1.0022	-0.78430

Analytical expressions for these constants can be obtained in a pure van der Waals potential, (i.e., $V^{lr} = -C_6/R^6$). Two linearly independent solutions of the single channel Schrödinger equation, $H = \partial^2/\partial R^2 + 2\mu C_6/R^6$, are given by

$$\begin{aligned} Y_1 &= R^{1/2} J_{-1/4}(x) \\ Y_2 &= R^{1/2} N_{-1/4}(x) \end{aligned} \quad (4.18)$$

where, again $x = \sqrt{\frac{\mu C_6}{2}} R^{-2}$ is a rescaled variable. Asymptotically expanding the Bessel J and Neumann N functions and requiring $W(f^0, g^0) = W(Y_1, Y_2)$ leads to

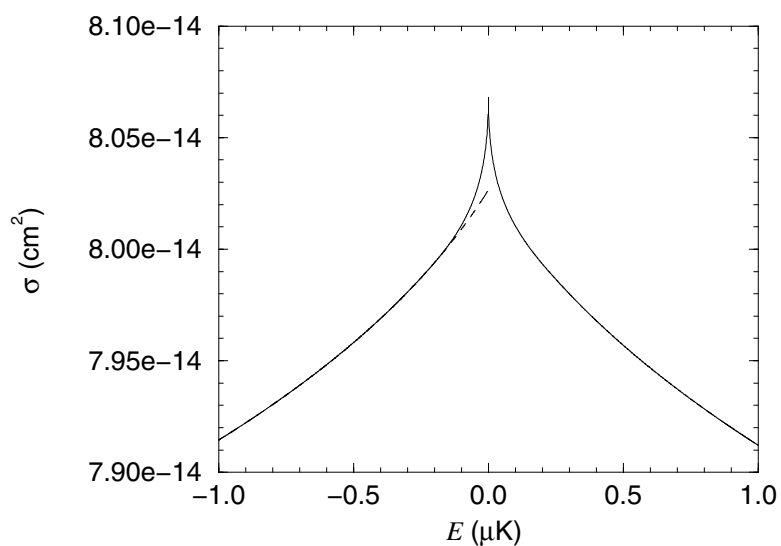


Figure 4.5: Energy dependence of the ${}^6\text{Li } f = 0(1/2, 1/2)$ elastic cross section. The collision complex is described by two channels which consist of both atoms being in either their $f_a = f_b = 1/2$ or $3/2$ hyperfine states. Zero energy indicates the position of the $3/2 + 3/2$ threshold. The ($E < 0$) solid line is a calculation using $\beta(0)$ from Eq. 4.17. The ($E < 0$) dashed line uses the numerical $\beta(0)$ which results in a slight artificial discontinuity in the energy dependence of the cross section.

the following expressions:

$$\begin{aligned}
 Y_1(R) &\rightarrow \frac{2\mu}{\pi k} \frac{2^{1/4}}{(2\mu C_6)^{1/8}} \sqrt{\frac{\Gamma(5/4)}{\Gamma(3/4)}} R \\
 Y_2(R) &\rightarrow -\frac{2\mu}{\pi k} \left(\frac{(2\mu C_6)^{1/8}}{2^{1/4}} \sqrt{\frac{\Gamma(3/4)}{\Gamma(5/4)}} + \frac{2^{1/4}}{(2\mu C_6)^{1/8}} \sqrt{\frac{\Gamma(5/4)}{\Gamma(3/4)}} R \right).
 \end{aligned} \tag{4.19}$$

Comparing equation 4.13 with 4.19 yields the following values for C^2 and $\mathcal{G}(0)$:

$$\begin{aligned}
 C^2 &= \frac{(2\mu C_6)^{1/4} \Gamma(3/4)}{\sqrt{2} \Gamma(5/4)} = 0.95598 (2\mu C_6)^{1/4} = \bar{a} \\
 \mathcal{G}(0) &= -1.0.
 \end{aligned} \tag{4.20}$$

This expression for C^2 is fairly well known, because it was derived previously in Ref[94]. Gribakin and Flambaum call this parameter the characteristic scattering length \bar{a} that appears in their semi-classical expression for the physical scattering length a . Also, the analytic constants derived from a pure van der Waals potential are very nearly equivalent to the numerical values that include the effects of higher order dispersion terms in V^{lr} (see Table 4.1). This gives us some indication as to why the standardization works as well as it does. Referring back to Fig. 4.2, the C_8 and C_{10} terms contribute little to the potential beyond $R \sim 35$ Bohr. Neglecting the higher order dispersion terms, the Schrödinger equation can be rescaled in terms of the dimensionless parameter γ , which in the process removes all atom specific information from the equation and therefore from the long-range parameters.

4.2 Constructing scattering matrices and wave functions

The procedure outlined in chapter 3 requires the integration of a set of $N = N_o + N_c$ coupled Schrödinger equations outward from the origin to some large internuclear distance of order $R \sim 10^3$ Bohr. However, we have now defined reference wave functions (f^0, g^0) that are mathematically correct solutions beyond $R_0 \geq 35$ Bohr. It is therefore only necessary to integrate the coupled Schrödinger equations to R_0 . The $N \times N$ solution matrix $\underline{M}(R)$ at a total energy E can be written as a linear combination of (f_i^0, g_i^0) at all radii $R \geq R_0$. These N independent solutions are standardized to have the following form:

$$\underline{M}(R) = \underline{f}^0(R) - \underline{g}^0(R) \underline{K}^{sr}, \quad R \geq R_0, \tag{4.21}$$

where $M_{ij}(R)$ is the i -th channel component of the j -th independent solution. Here f_i^0 and g_i^0 are diagonal matrices in the channel space, evaluated at the appropriate channel energy $\varepsilon_i = E - E_i$, with E_i the dissociation threshold energy, and l_i

the relevant orbital momentum in the i -th channel. The solution matrix still has components in energetically closed channels, but this method usually works best if all channels included at $R \geq R_0$ are still “locally open”, i.e. with $k^2(R_0) > 0$. The short range (atom-dependent) physics is completely encapsulated in the short range reaction matrix $\underline{K}^{\text{sr}}$, which varies slowly with E or B , except near isolated poles. The weak energy- and field-dependence of $\underline{K}^{\text{sr}}$ is illustrated in Fig. 4.6.

The solution matrix (Eq. 4.21) does not yet satisfy the proper asymptotic scattering boundary conditions. In particular, \underline{M} still contains closed channels. The asymptotic boundary conditions for these channels must be imposed in a simple matrix manipulation at each desired final state energy, through the following procedure[23]. First partition the $\underline{K}^{\text{sr}}$ matrix into N_o open channels (those channels $i \in P$, for which $\varepsilon_i = E - E_i \geq 0$) and N_c closed channels ($i \in Q$, for which $\varepsilon_i = E - E_i < 0$). In this notation, $\underline{K}^{\text{sr}}$ becomes:

$$\underline{K}^{\text{sr}} = \begin{pmatrix} \underline{K}_{PP}^{\text{sr}} & \underline{K}_{PQ}^{\text{sr}} \\ \underline{K}_{QP}^{\text{sr}} & \underline{K}_{QQ}^{\text{sr}} \end{pmatrix}. \quad (4.22)$$

The exponentially-growing parts of the wave functions at $R \rightarrow \infty$ are next “eliminated” by applying a $N \times N_o$ transformation matrix $\underline{B}(E)$,

$$\underline{B} = \begin{pmatrix} \underline{1} \\ -(\tan \underline{\beta} + \underline{K}_{QQ}^{\text{sr}})^{-1} \underline{K}_{QP}^{\text{sr}} \end{pmatrix} \quad (4.23)$$

where $\underline{1}$ represents an $N_o \times N_o$ identity matrix and $\tan \underline{\beta}$ is a diagonal matrix of the negative energy phases defined in the preceding section (4.1.2), evaluated at the appropriate channel energy $\varepsilon_i = E - E_i$. This transformation correctly assembles the linear combination of independent solutions which forces the closed channel components of the wave function to zero as $R \rightarrow \infty$. The open channel subspace of the new “physical” solution matrix $\underline{F}^0 = \underline{M} \underline{B}$ is given by:

$$\underline{F}^0(E, R) = \underline{f}^0 - \underline{g}^0 \underline{\tilde{K}}. \quad (4.24)$$

The modified reaction matrix $\underline{\tilde{K}}$ has dimensions $N_o \times N_o$ and contains the potentially resonant influence of closed-channel pathways:

$$\underline{\tilde{K}} = \underline{K}_{PP}^{\text{sr}} - \underline{K}_{PQ}^{\text{sr}} (\underline{K}_{QQ}^{\text{sr}} + \tan \underline{\beta})^{-1} \underline{K}_{QP}^{\text{sr}}. \quad (4.25)$$

Moreover, should all channels be closed, discrete bound states occur at roots of the following determinantal equation:

$$\det (\underline{K}_{QQ}^{\text{sr}} + \tan \underline{\beta}) = 0. \quad (4.26)$$

Since $\underline{K}^{\text{sr}}$ is only weakly-energy dependent and $\beta(\varepsilon)$ has been tabulated for the long-range potential of interest, the search for bound states and resonances is easy.

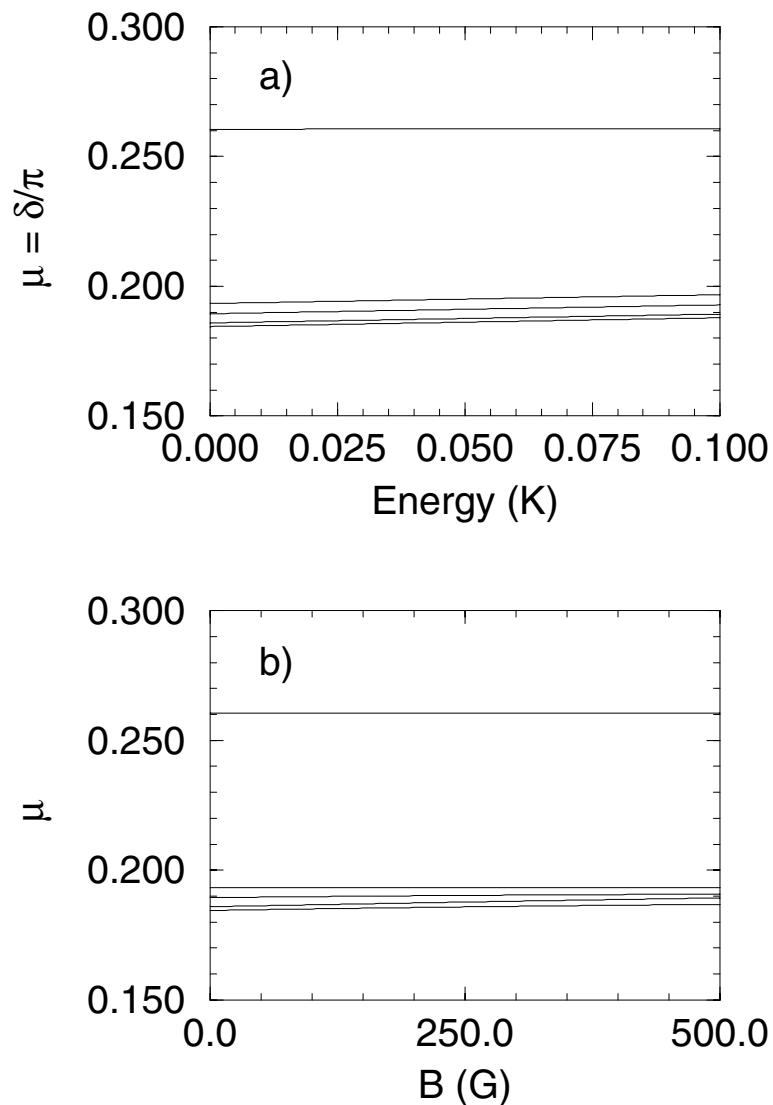


Figure 4.6: The eigenvalues of the short-range matrix $\underline{K}^{\text{sr}}$ are plotted as functions of a) energy and b) magnetic field. The eigenvalues of the reaction matrix, $\tan \delta_\lambda$, are known as eigenphase shifts and these have been converted into quantum defects through the relation $\mu_\lambda = \delta_\lambda/\pi$. In both cases, the quantum defects are nearly constant implying that $\underline{K}^{\text{sr}}$ can be treated, to a very good approximation, as constant over this range of energy and magnetic field. This particular example is for the collision of two $|2, -2\rangle$ ^{85}Rb atoms.

We want the final scattering solutions to be energy-normalized. This is accomplished by first relating the energy-analytic base pair (f^0, g^0) to the energy-normalized pair (f, g) (using Eq. 4.8):

$$\underline{F}(E, R) = [\underline{f} - \underline{g} \underline{K}] . \quad (4.27)$$

(The solution matrices $\underline{F}^0(E, R)$ and $\underline{F}(E, R)$ are related by an R -independent matrix $\underline{C}(E) = \underline{A}^{1/2}(\underline{1} + \underline{G} \underline{\tilde{K}})$, i.e. $\underline{F}^0(E, R) = \underline{F}(E, R)\underline{C}(E)$, which can be ignored since it has no bearing on the final determination of the scattering matrix.) The new $N_o \times N_o$ real, symmetric, “energy-normalized” reaction matrix in the (f, g) representation is obtained using[82]

$$\underline{K} = \underline{A}^{1/2} \left(\underline{\tilde{K}}^{-1} + \underline{G} \right)^{-1} \underline{A}^{1/2} . \quad (4.28)$$

This is still not quite the “physical” reaction matrix $\underline{K}^{\text{phys}}$ of conventional scattering theory, owing to the phase shift $\eta(\varepsilon, l)$ of (f, g) relative to (j_l, n_l) at $R \rightarrow \infty$. Nevertheless, \underline{K} possesses other properties expected in $\underline{K}^{\text{phys}}$, such as the Wigner threshold behavior which is reflected in the dependence $A(\varepsilon, l) \sim \varepsilon^{l+1/2}$ as $\varepsilon \rightarrow 0$. $\underline{A}^{1/2}$ and \underline{G} are diagonal matrices in channel space, again evaluated at the appropriate channel energy $\varepsilon_i = E - E_i$. At this stage, it is a simple matter to construct the “physical” scattering matrix \underline{S} . A scattering matrix in the (f, g) representation can be obtained by the relationship given in Eq. 3.18. The additional phase shift of (f, g) relative to (j_l, n_l) is then accounted for when the physical scattering matrix is determined in the following manner,

$$\underline{S} = e^{i\eta} \frac{1 + i\underline{K}}{1 - i\underline{K}} e^{i\eta} . \quad (4.29)$$

Here, $\underline{\eta}$ is a diagonal matrix. The final \underline{S} -matrix is given completely in terms of the short-range reaction matrix $\underline{K}^{\text{sr}}$ and the four long range parameters $A(\varepsilon, l)$, $\mathcal{G}(\varepsilon, l)$, $\eta(\varepsilon, l)$, and $\beta(\varepsilon, l)$.

Fig. 4.7 compares the elastic s -wave partial cross section calculated with the “essentially exact” FEM \underline{R} -matrix approach and a quantum defect calculation performed with an energy-independent $\underline{K}^{\text{sr}}$ via equations 4.25, 4.28, and 4.29. The MQDT results quantitatively reproduce all features of the spectrum over tens of mK with a single $\underline{K}^{\text{sr}}$ calculated at $E=0$, relative to the 2+2 threshold. This calculation also predicts the energy of the zero-field Feshbach resonance[17, 16] (near 29 mK) to an accuracy of ≈ 0.1 mK. The small shift in the resonance position indicates that $\underline{K}^{\text{sr}}$ is not strictly constant over this energy range. Effects associated with this slight energy dependence can be incorporated by interpolation of $\underline{K}^{\text{sr}}$ after it is tabulated on a coarse energy grid.

Energy normalized scattering wave functions will be needed for the pho-

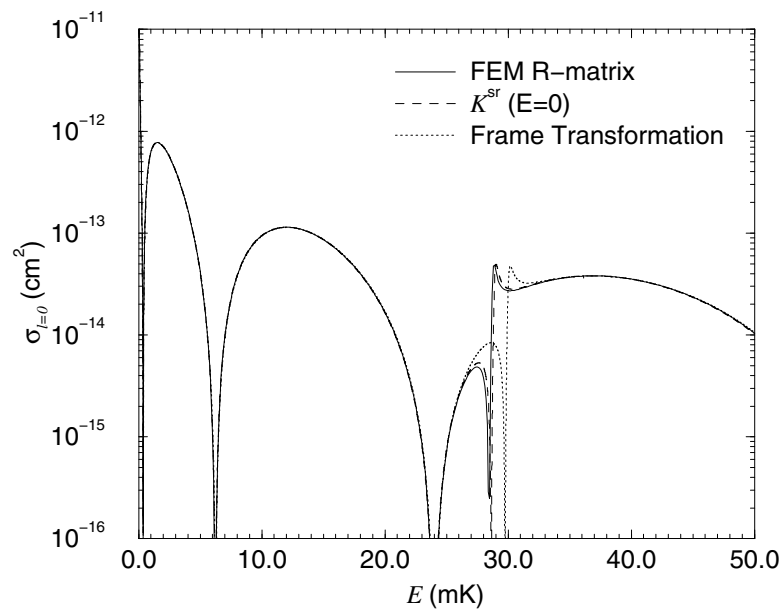


Figure 4.7: Elastic s -wave partial cross section for the collision of two ^{85}Rb atoms in their $|2, -2\rangle$ atomic hyperfine states. The feature near 29 mK is the zero-field position of the Feshbach resonance observed in Refs.[17] and [16]. The solid curve is a FEM \underline{R} -matrix calculation. The dashed curve is an MQDT calculation using a constant $\underline{K}^{\text{sr}}$ calculated at $E=0$. The short dashed line is a calculation using the energy-dependent frame transformation approximation for $\underline{K}^{\text{sr}}$.

toassociation study in Chapter 7, in the range beyond $R \geq 30$ Bohr. This is achieved by right-multiplication of Eq. 4.27 using a normalization matrix \underline{N} that transforms the wave function into scattering matrix states (i.e., incoming and outgoing waves) that satisfy the asymptotic boundary condition given in Eq. 2.4. The energy-normalized standing-wave base pair (f, g) are defined in terms of the energy-normalized traveling-wave base pair (f^+, f^-) through the following relationships[23]:

$$f_i = \frac{f_i^+ - f_i^-}{\sqrt{2}i} \quad (4.30)$$

$$g_i = \frac{-f_i^+ - f_i^-}{\sqrt{2}}, \quad (4.31)$$

and the base pair (f^+, f^-) are defined as:

$$f_i^+ = \sqrt{\frac{2\mu}{\pi\hbar^2 k_i}} \frac{e^{i(k_i R - l_i \pi/2)}}{\sqrt{2}} \quad (4.32)$$

$$f_i^- = \sqrt{\frac{2\mu}{\pi\hbar^2 k_i}} \frac{e^{-i(k_i R - l_i \pi/2)}}{\sqrt{2}}. \quad (4.33)$$

Substituting (f_i^+, f_i^-) for (f_i, g_i) into Eq. 4.27 and requiring $(\underline{F}\underline{N})_{ii'}$ to equal the asymptotic boundary condition in Eq. 2.4, we find the following expression for the normalization matrix:

$$\underline{N} = (\underline{1} - i\underline{K})^{-1}. \quad (4.34)$$

An energy-normalized radial solution valid beyond $R \geq 35$ Bohr is then represented by

$$\underline{\Psi}(E, R) = \underline{F}(E, R)\underline{N}(E). \quad (4.35)$$

Generation of these wave functions requires only $\underline{K}^{\text{sr}}$, the four long-range MQDT parameters, and the single channel reference wave functions (f^0, g^0) . In the case of a single open channel there is an alternative real representation for $\underline{\Psi}$ that is useful and is given by:

$$\underline{\Psi}(E, R) = \underline{F}^0(E, R)N^0(E). \quad (4.36)$$

Here, $\underline{F}^0(E, R)$ is given by Eq. 4.24 and the normalization constant is equal to the following expression:

$$N^0(E) = \frac{\sin \delta^r}{A^{1/2} \tilde{K}} \quad (4.37)$$

where $\delta^r = \tan^{-1}(K)$.

Finally, we can derive a formula that connects the single channel scattering length a with the MQDT parameters. The physical phase shift is given in terms of the MQDT parameters by $\delta = \delta^r + \eta_i$. In this context δ^r represents the phase shift relative to (f, g) which in the zero energy limit is equivalent to the physical phase shift, $\delta^r = \delta$. The scattering length $a = -\tan \delta/k$ can therefore be written in terms of the long-range parameters as follows

$$a = \frac{-C^2 \tilde{K}}{1 + \mathcal{G}(0) \tilde{K}} \quad (4.38)$$

where the low energy behavior of the parameter $A \rightarrow C^2 k$ has been incorporated.

4.3 Frame transformation approximation

At this stage, the theory presented still requires a full solution of the coupled radial Schrödinger equations to obtain $\underline{K}^{\text{sr}}$. However, as discussed in section 3.3 the dominant spin exchange coupling is localized in the range $R \sim 25$ Bohr (see Fig. 3.2). To a good approximation the atoms move at $R \lesssim 20$ a.u. in a set of uncoupled channels, labeled by their total electronic spin quantum number S . We can therefore integrate the single channel Schrödinger equations with all hyperfine interactions omitted, after which each solution can be matched to the energy-analytic base pair (f^o, g^o) to obtain singlet ($S=0$) and triplet ($S=1$) quantum defects $\mu_S(\varepsilon)$. (The quantum defects μ_S are related to the singlet or triplet phase shift by $\mu_S = \delta_S/\pi$. The phase shift is given in terms of the single channel short-range reaction matrix by $\delta = \tan^{-1} \underline{K}^{\text{sr}}$.) The short range reaction matrix is then approximated by the frame transformation (FT) formula

$$K_{i,i'}^{\text{sr}} = \sum_{\lambda} \langle i|\lambda \rangle \tan \pi \mu_{\lambda}(\bar{\varepsilon}_{\lambda}) \langle \lambda|i' \rangle. \quad (4.39)$$

Here $X_{i\lambda} = \langle i|\lambda \rangle$ represents the unitary transformation matrix that connects the short range singlet-triplet basis $|\lambda \rangle \equiv |(s_a, s_b)S(i_a, i_b)I FM \rangle$ with the asymptotic hyperfine basis $|i \rangle \equiv |(s_a, i_a)f_a(s_b, i_b)f_b FM \rangle$. $X_{i\lambda}$ is understood to be the transformation matrix between **symmetrized** kets if the particles are identical. These transformations are discussed in section 2.3.2. One important point to note is that the FT approximation for $\underline{K}^{\text{sr}}$ includes energetically closed channels as in previous MQDT studies[23]. Therefore, our FT approximation includes the Feshbach resonance physics which distinguishes it from a related class of approximations (notably the degenerate internal states method of cold collisions[95, 96], or equivalently the adiabatic nuclei method[97, 98, 99] of electron-molecule scattering theory). We have tried two different implementations of the frame transformation approximation. The first and simplest is an **energy-independent** approximation which uses

only the zero energy values of the quantum defects (i.e., $\bar{\varepsilon}_\lambda = 0$ in Eq. 4.39). In a different implementation of the **energy-dependent** FT than used previously, the energy $\bar{\varepsilon}_\lambda$ at which μ_λ is calculated in Eq. 4.39 is chosen to be a weighted average of the channel energies ε_i appropriate for eigenchannel $|\lambda\rangle$, i.e. $\bar{\varepsilon}_\lambda \equiv \sum_i \varepsilon_i |\langle i|\lambda\rangle|^2$. In tests conducted to this point, the energy-independent FT approximation has proven to be more accurate for the diagonal (elastic) \underline{S} -matrix elements, while the energy-dependent FT approximation has been more accurate for the off-diagonal (inelastic) \underline{S} -matrix elements. However, the quantum defects have only a weak energy-dependence (see Fig. 4.8) so neither approach has been remarkably better than the other. Given the greater simplicity of the energy-independent FT approximation, I would recommend it above the other approach. In particular, only two parameters are needed to determine $\underline{K}^{\text{sr}}$. The physical scattering matrix can then be obtained via equations 4.25, 4.28, and 4.29 as before, but now solely in terms of single channel quantities. Examples of the FT approximation are provided in the next section.

As a last item, the quantum defect can be related to the scattering length. In general, it is more useful to parameterize the singlet and triplet Born-Oppenheimer potentials in terms of their quantum defect rather than their scattering length as is commonly done. For one thing, the complete range is covered over $\pm 1/2$ and accordingly they never experience a pole as scattering lengths can. But more importantly, given the quantum defects one can calculate an \underline{S} -matrix that is reasonably accurate for the entire range of energy and field relevant for cold collisions. This is in contrast to the scattering length, which only allows one to predict an s -wave elastic cross section over a very limited energy range ($E \sim 0$ -few tens of μK in Rb). Returning to the scattering length equation (Eq. 4.38) and substituting in the quantum defect for \tilde{K} gives the relationship between a and μ :

$$a = \frac{-C^2 \tan \pi \mu}{1 + \mathcal{G}(0) \tan \pi \mu} . \quad (4.40)$$

This equation is readily inverted to express μ as a function of a :

$$\mu = \frac{1}{\pi} \tan^{-1} \left[\frac{-a}{C^2 + a \mathcal{G}(0)} \right] . \quad (4.41)$$

From this equation we find the following correspondence between the ranges of a and μ :

$$\begin{aligned} a = 0 & \quad , \quad \mu = 0 \\ a < 0 & \quad , \quad 0 < \mu < \frac{1}{\pi} \tan^{-1} \left[\frac{-1}{\mathcal{G}(0)} \right] \\ a = +\infty & \quad , \quad \mu = \frac{1}{\pi} \tan^{-1} \left[\frac{-1}{\mathcal{G}(0)} \right] . \end{aligned} \quad (4.42)$$

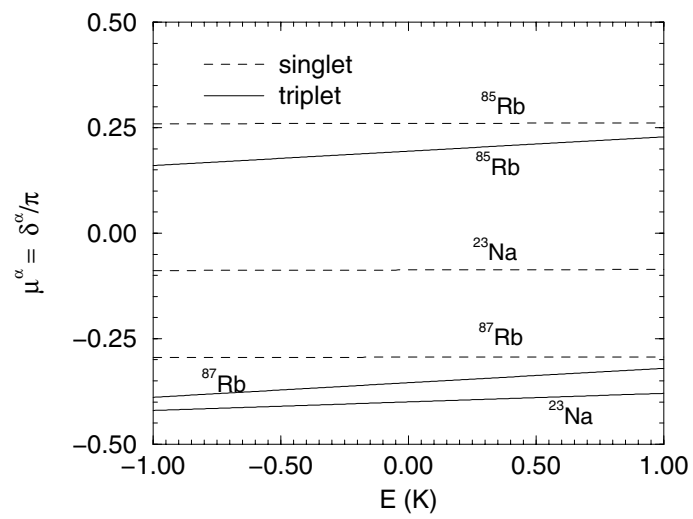


Figure 4.8: The weak energy-dependence of the Rb and Na singlet and triplet quantum defects are shown. The minimum of the triplet potential is not as deep as the singlet (see Fig. 2.1) and therefore the triplet quantum defects are a little more energy-dependent.

Values for $\mathcal{G}(0)$ are given in Table 4.1, from which we can see that a negative scattering length corresponds to $0 < \mu \lesssim 0.25$. All other values of μ (within its defined range) correspond to a positive scattering length. Given no information about the ground state Born-Oppenheimer potential, Gribakin and Flambaum’s semi-classical theory[94] predicts that there is a 75% chance that a van der Waals potential will have a positive scattering length. We can find the deviation from this number caused by the inclusion of higher order dispersion terms in the potential by comparing the range of μ for which a is positive with the total allowed range of μ , which is $\sim 0.751/1.0$. Therefore a potential which includes the higher order dispersion terms has approximately a 75.1% chance of having a positive scattering length.

4.4 Examples

We have verified that no accuracy is lost in our \underline{S} -matrix calculated when the multichannel solutions are represented beyond $R = 35$ Bohr by the semianalytic long-range reference functions (f_i^0, g_i^0) , rather than the FEM \underline{R} -matrix solution. However, if it required calculating $\underline{K}^{\text{sr}}$ at each energy and field, the method would not be that much of an improvement over the brute force numerical approach. The real utility of the MQDT method comes from the fact that $\underline{K}^{\text{sr}}$ can be treated, to a good approximation, as constant in energy and field and therefore only needs to be calculated once. Moreover, the frame transformation approximation allows $\underline{K}^{\text{sr}}$ to be calculated solely in terms of two single channel quantum defects and a standard recoupling matrix. The accuracy of this approach has already been illustrated in Fig. 4.7. Both approximations produce elastic s -wave partial cross sections that agree within 2% of the FEM \underline{R} -matrix calculations over a 50 mK energy range except near the zero-field Feshbach resonance. The discrepancy in the energy position of the resonance is ≈ 0.1 mK with a constant $\underline{K}^{\text{sr}}$ and by ≈ 1.4 mK in the energy-dependent FT approximation. This will generally be the case. Both approximations for $\underline{K}^{\text{sr}}$ produce accurate \underline{S} -matrices provided no resonances or quantum interferences are present. Using an approximate $\underline{K}^{\text{sr}}$ will still predict these quantum effects but at an energy or field value slightly shifted from its true location. This is examined in more detail in the examples below. (The possibility exists that our method could predict shape resonances that are either spurious or at the wrong energy but we have seen no evidence for this in the partial waves ($l=1-4$) examined to date. This could occur if the reference potential $V^{lr} + l(l+1)/(2\mu R^2)$ supported a shape resonance.)

Fig. 4.9 shows the magnetic field-induced Feshbach resonance measured in Ref.[17]. Four methods have been used to calculate the scattering length a . The FEM \underline{R} -matrix is considered to be the “exact” solution with a resonance position (defined here to be simply where $a \rightarrow \infty$) of $B_r = 155.4$ G. The second method uses a $\underline{K}^{\text{sr}}$ calculated at $E = 0, B = 0$. The reaction matrix $\underline{K}^{\text{sr}}$ is rotated into the representation in which the asymptotic Hamiltonian is diagonal at each B (see

section 2.3) and then equations 4.25, 4.28, and 4.29 are used to produce the final \underline{S} -matrix from which the scattering length is extracted (Eq. 2.34). Treating $\underline{K}^{\text{sr}}$ as independent of E and B predicts a resonance field value of $B_r = 156.4$ G, which is shifted 1 Gauss higher than its true location. The other two methods are the energy-dependent and energy-independent FT approximations. These predict resonance field values B_r equal to 161.8 G and 156.1 G, respectively. The predicted resonance field value from the energy-independent FT is actually more accurate than the one using a multichannel calculation for the constant $\underline{K}^{\text{sr}}$, although this is probably just an accident. The coupled-channel version of $\underline{K}^{\text{sr}}$ produces more accurate off-resonance values for a . Finally the resonance is shown again in Fig. 4.10, which test our standardization of the long-range parameters. Here, both calculations use the same $\underline{K}^{\text{sr}}(E = 0, B = 0)$ as in the previous graph. Two sets of standardized long-range parameters are used, one calculated with ^{39}K atomic properties (i.e., mass and dispersion coefficients) and the other with ^{85}Rb properties (these were used in the previous figure). The off-resonance values of a agree to within $\sim 1\%$. However, the calculation with the ^{39}K standardized parameters predicts a resonance field position of $B_r = 136.2$ G.

^{87}Rb inelastic loss rates are examined in Fig. 4.11. Again, four different methods have been used, and we regard the FEM \underline{R} -matrix calculation as providing the “exact” benchmark rates. Here, we see that treating $\underline{K}^{\text{sr}}$ as constant in energy reproduces the inelastic rates to within 7% over a 10 mK energy range. However, in this example the FT approximations are disastrous. This is because the ^{87}Rb singlet a_s and triplet a_t scattering lengths are nearly equivalent producing a suppressed inelastic rate. This suppressed spin-exchange rate was observed in Ref.[100]. The FT approximation will predict suppressed inelastic rates but only when $a_s \simeq a_t$ (the equality holds exactly for the energy-independent FT). The ^{87}Rb inelastic scattering rates are discussed in more detail in Section 5.1. The range over which the FT will provide realistic inelastic rates is examined in Fig. 4.12. Here, the percentage difference of an off-diagonal mod-squared S -matrix element calculated with the energy-independent FT approximation and with the FEM \underline{R} -matrix method are compared over the entire ^{23}Na $\mu_s - \mu_t$ plane. There are no closed channels in this particular case of scattering from an $f = 2(2, 2)$ total spin state into an $f = 2(1, 1)$ state. The FT approximation agrees to within 10% of the exact value over most of the parameter space. The exception is along the line of suppressed rates $\mu_s \simeq \mu_t$, just as with ^{87}Rb collisions. The presence of resonances associated with closed channels will modify these results just as it did with elastic scattering. The accuracy of the FT diminishes somewhat with increased hyperfine splitting and with increased mass. At present, it has not been used for Cs calculations but the FT does in general, produce excellent results for Li through Rb with the few exceptions noted in this section.

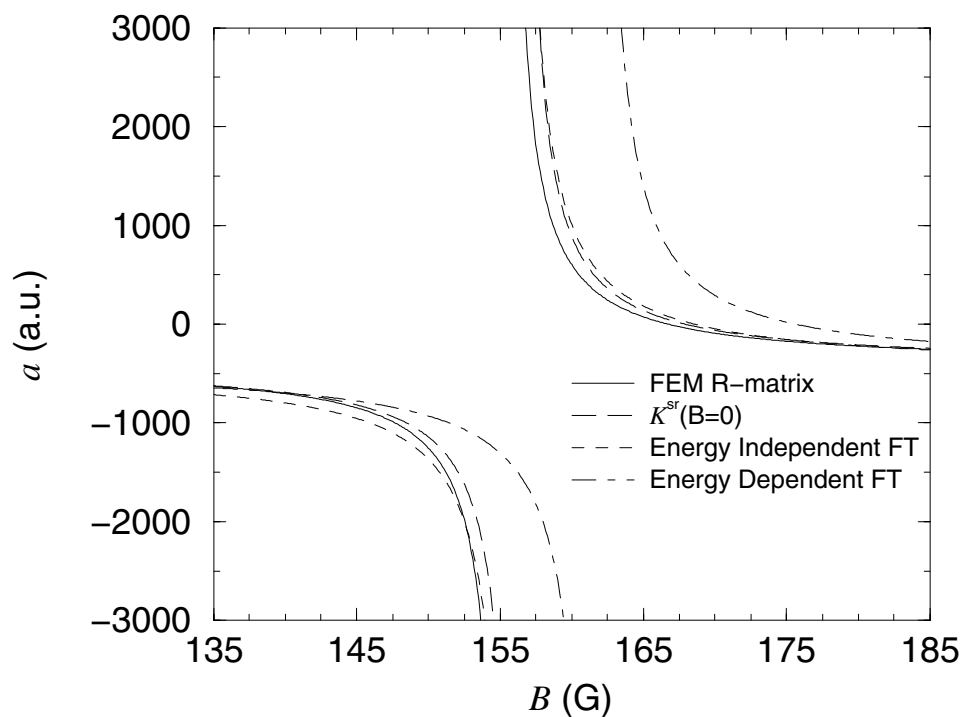


Figure 4.9: Scattering length a versus magnetic field B for the collision of two ^{85}Rb atoms both of which are in their $|2, -2\rangle$ hyperfine state. Three methods using an approximate $\underline{K}^{\text{sr}}$ are compared with an “exact” FEM \underline{R} -matrix calculation. The FEM \underline{R} -matrix approach predicts the Feshbach resonance field position in accordance with Ref.[17]’s measurement. The collision energy was taken to be $E = 1 \mu\text{K}$.

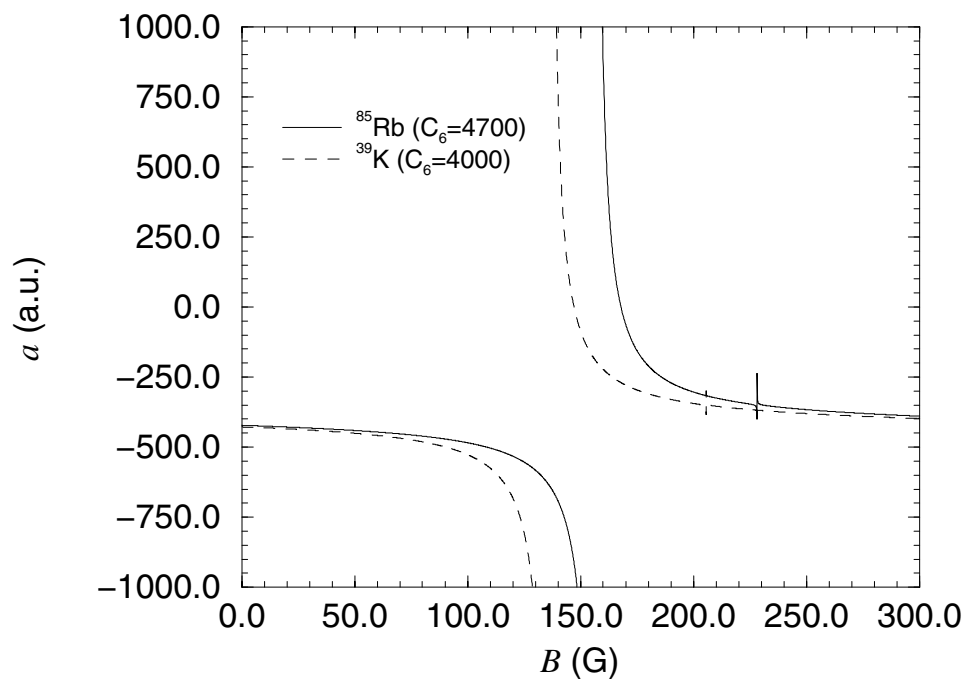


Figure 4.10: Scattering length a versus magnetic field B for the collision of two ^{85}Rb atoms both of which are in their $|2, -2\rangle$ hyperfine state. A constant $\underline{K}^{\text{sr}}$ calculated at $E = 0$, $B = 0$ is used for both calculations. One (solid line) uses long-range standardized parameters calculated with ^{85}Rb atomic properties. The other (dashed line) uses long-range standardized parameters calculated with ^{39}K atomic properties. The collision energy was taken to be $E = 1 \mu\text{K}$.

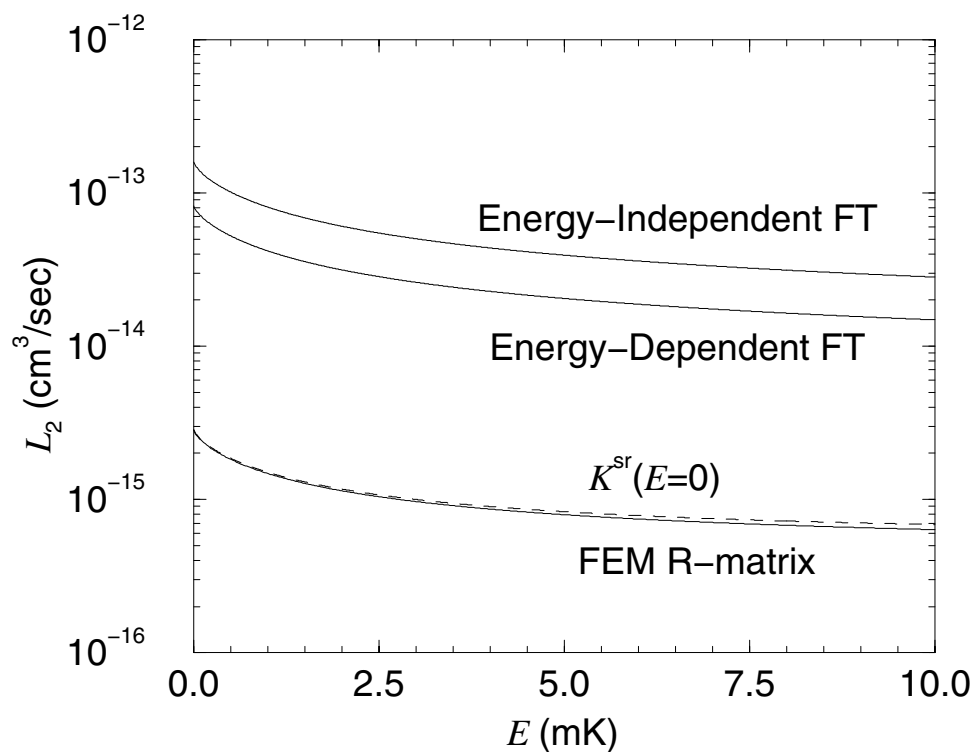


Figure 4.11: The total inelastic loss rate L_2 for a $|2, 2\rangle_{87} + |1, -1\rangle_{87}$ collision. Calculations using an approximate \underline{K}^{sr} are compared with the exact rates determined from a FEM \underline{R} -matrix solution.

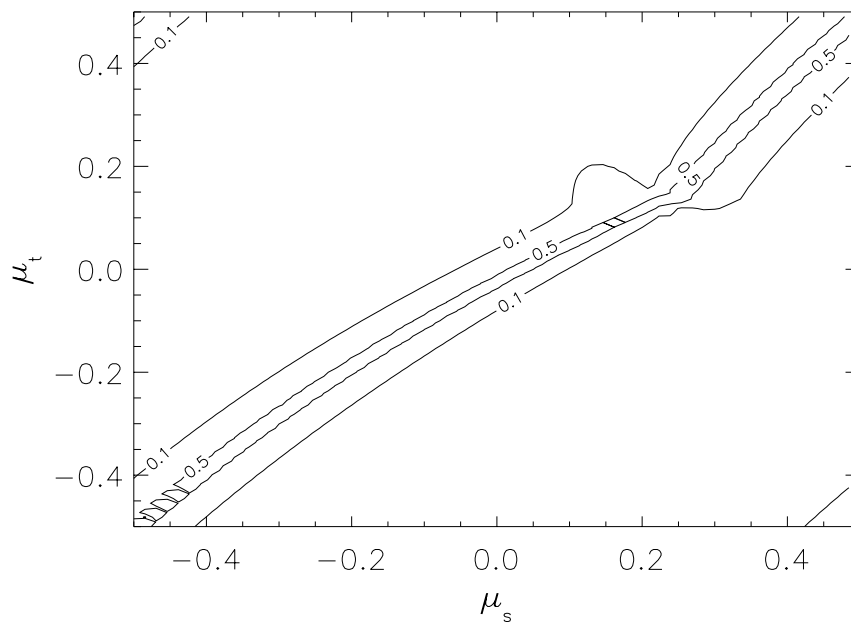


Figure 4.12: Mod-squared off-diagonal S -matrix elements calculated with an energy-independent FT approximation and with the FEM R-matrix approach are compared in this contour plot. These matrix elements are plotted as the absolute value of the percentage difference. The 0.1 = 10% and 0.5 = 50% contour lines are shown. The mod-squared S -matrix element for this particular case represents the transition probability $f = 2(f_a = 2, f_b = 2) \rightarrow 2(1, 1)$ in the collision of two Na atoms. The physical values of the Na quantum defects are $\mu_s = -0.087$ and $\mu_t = -0.400$.